22.12.2015

Supporting information

Synthesis and three-dimensional magnetic field mapping of Co$_2$FeGa Heusler nanowires at 5 nm resolution

Paul Simon[a*], Daniel Wolf[b], Changhai Wang[a], Aleksandr A. Levin[a], Axel Lubk[b], Sebastian Sturm[b], Hannes Lichte[b], Gerhard H. Fecher[a], Claudia Felser[a]

[a] *Max-Planck-Institut für Chemische Physik fester Stoffe, Nöthnitzer Str. 40, 01187 Dresden, Germany*

[b] *Institute of Structure Physics, Triebenberg Laboratory, Technical University of Dresden, Zum Triebenberg 50, 01328 Dresden Zaschendorf, Germany*

- Experimental details with references

  1.1 Synthesis

  1.2 Small-angle and wide-angle X-ray diffraction

  1.3 Scanning electron microscopy and energy-dispersive X-ray spectroscopy

  1.4 X-ray absorption near-edge structure and extended X-ray absorption fine structure spectroscopy

  1.5 TEM techniques

  1.6 Fidelity of EHT reconstructions

- Figure S1   Scheme of the chemical synthesis of Co$_2$FeGa nanowires

- Figure S2   Small-angle X-ray scattering; SEM and TEM of SBA15

- Figure S3   SEM and TEM images of Co$_2$FeGa nanowires grown on silica template SBA15

- Figure S4   EDX

- Figure S5   XANES

- Figure S6   EXAFS

- Figure S7   EELS and EFTEM

- Figure S8   Holography (2D)

- Figure S9   Procedure for analysis and partial correction of missing wedge artefacts

- Figure S10   Effect of diffraction contrast

- Movie 1   Hologram tilt series

- Movie 2   Reconstructed phase tilt series

- Movie 3   3D electrostatic potential

1. Experimental details

1.1 Synthesis

All chemicals were purchased from Sigma-Aldrich and used as received. The nonionic triblock copolymer, Pluronic P123 (MW 5800), was utilized as so called structure-directing surfactant. Tetraethoxysilane (TEOS) was used as a silicon source. The precursors for Co-Fe-Ga nanocrystals were $Fe(NO_3)_3 \cdot 9H_2O$ (99.99%), $CoCl_2 \cdot 6H_2O$ (100%) and $Ga(NO_3)_3 \cdot xH_2O$ (99.9%). In accordance with references [1,2], the value of x in $Ga(NO_3)_3 \cdot xH_2O$ was set to 8 for calculations.

The preparation of mesoporous SBA-15 silica followed the procedures reported in Ref. [3]. In a typical preparation, 4.0 g of Pluronic P123 was dissolved in a solution consisting of 30 g of water and 120 ml of HCl (2 M) at 35-40 °C after overnight stirring. Then 8.5 g of TEOS was added to the clear solution with robust stirring at the same temperature for 24 h. The milky suspension was then transferred to a 250 ml polypropylene storage bottle and hydrothermally

treated at 80 °C for 24 h. The solid product was recovered, washed with deionized water, and air-dried at room temperature in the chemical hood. To remove the structure-directing agents, the dried SBA-15 powders were heated to 500 °C with a slow ramp (1 °C/min) and annealed for 6 h.

To prepare the Co_2FeGa/SBA-15 nanocomposite, 0.44 mmol of $Fe(NO_3)_3 \cdot 9H_2O$, 0.49 mmol of $CoCl_2 \cdot 6H_2O$ and 0.32 mmol of $Ga(NO_3)_3 \cdot xH_2O$ were dispersed in 50 ml of methanol and treated with a mild sonication for 10 min. Subsequently, 1 g of SBA-15 silica was added to the precursor solution and the suspension was sonicated for another 20 min. Methanol was removed using a rotary evaporator. The obtained solid was then dried at 80 °C overnight to achieve complete dryness. The solid was gently ground to powder and typically 200 mg was used for annealing (850 °C for 2 h) under H_2 atmosphere with a flow rate of 50 ml/min (see Figure S1).

1.2 Small-angle and wide-angle X-ray diffraction

The crystal structure of Co_2FeGa/SBA-15 nanocomposites was investigated by powder X-ray diffraction (XRD) technique using X'Pert PRO diffractometer (PANalytical B.V., Nederlands) designed in focusing Bragg-Brentano geometry and supplied with solid state X'Celerator linear detector. Cu-$K_{\alpha 1}$ radiation monochromatized by a primary Ge(111) monochromator of Johansson type was used. Small-angle X-ray scattering (SAXS) measurements were conducted using the same diffractometer to resolve the dimension and ordered structure characteristics of SBA-15. The SAXS pattern of the SBA-15 powder recorded is presented in Figure S2d. The XRD and SAXS patterns were corrected to $\Delta 2\theta_{zero}$ shift using Si 640c and mica 675 NIST powder standards [4] and to substrate contribution. The calculated lattice parameter of the hexagonal plane lattice ($a = 105.8(7)$ Å, plane group *p6mm* (No. 17)) is in a good agreement with the typical unit cell parameters reported for synthetic SBA-15 [3]. During the calculations, the $2\theta_{Bragg}$ central angle-positions of the observed Bragg reflections were corrected to refraction shift [5] which becomes essential for SAXS.

The wide angle XRD pattern exhibits an amorphous halo due to amorphous mesoporous SBA-15 silica and XRD reflections attributed to cubic Co_2FeGa *Heusler* phase (Figure 1f of the main article). Even though the applied Cu-$K_{\alpha 1}$ radiation causes a high fluorescence of Fe containing

compounds, the weak reflections unique for $L2_1$ Co$_2$FeGa *Heusler* phase still were clearly resolved (see inset in Figure 1f) confirming the presence of this structure. The unit cell parameter of cubic Co$_2$FeGa compound calculated from the indexed reflections by means of program CelSize [6] (a = 5.7372(14) Å) was close to the unit cell parameter of the ideal Co$_2$FeGa phase (*a* = 5.737 Å for Co$_2$FeGa [7] in comparison to *a* = 5.767 Å for Fe$_2$CoGa [8]).

A Rietveld fitting of the experimental XRD pattern was carried out by means of program WinCSD [9]. In the $L2_1$ structure (space group $Fm\bar{3}m$ (No. 225)), all atoms are fixed in special crystallographic positions. The occupation factors of atomic positions were fixed to unity during the refinement (i.e. ideal Co$_2$FeGa composition was used). The refined atomic isotropic temperature displacement parameters (B_{iso} = 1.47(3), 1.46(3) and 1.60(3) Å^2 for Fe, Co and Ga, respectively) were close to each other. In the limits of estimated standard deviations (e.s.d.), the refined unit cell parameter (a = 5.7412(1) Å) is the same as the lattice parameter directly calculated from the indexed reflections. The e.s.d. values for a and B_{iso} obtained in Rietveld refinement are corrected to underestimating due to serial correlations [10] by multiplication on coefficient $m_{e.s.d.}$ = 1.50 calculated by program RietEsd [11]. The reached agreement factors and statistics characteristics calculated according to [12] definitions are R_{wp} = 1.51 % (weighted profile factor, weight w = 1/y_{obs}), R_{exp}= 1.63 % (expected weighted profile factor), R_p = 1.17 % (profile factor), R_B = 3.16 % (Bragg factor), DWD = 1.22 (Durbin-Watson statistics).

1.3 Scanning electron microscopy and energy-dispersive X-ray spectroscopy

Scanning electron microscopy (SEM) and energy-dispersive X-ray spectroscopy (EDX) investigations were performed by means of an ESEM FEI Quanta 200 FEGi system (FEI company, Eindhoven, NL) operated in high vacuum mode. An acceleration voltage of 25 kV was utilized for SEM and EDX. For the investigations, samples were deposited from an ethanol suspension on copper TEM grids and measured on the aluminium SEM holder. SEM images exhibit an existence of extended areas of nanowire surrounded by particle agglomerates. Figures S2a-c, S3a-f and S4a present SEM and TEM images, illustrating the typical morphology of the

SBA-15 silica, the growth process of Co_2FeGa on the SBA-15 template and the typical morphology of Co_2FeGa nanowires after the etching, respectively.

A characteristic EDX spectrum of the Co_2FeGa nanowires is given in Figure S4b. The observed intensities of *L*-lines of elements were used for composition quantification of individual nanowires and particles. The mean composition of the nanowires was evaluated as $Co_{2.09(7)}Fe_{0.91(7)}Ga_{0.90(4)}$ (averaging on 19 different nanowires) close to ideal $L2_1$ Co_2FeGa composition. Additionaly, different types of particles were identified with mean compositions $Co_{1.00(4)}Fe_{0.73(4)}Ga_{0.25(3)}$ (2 particles, CoFe-like), $Co_{2.63}Fe_{0.05}Ga_{1.0}$ (1 particle, Co_3Ga-like) and $Co_{0.84}Fe_{0.06}Ga_{0.10}$ (1 particle, Co-like). The *L*-lines provided the ideal composition in the EDX whereas the evaluation of the *K*-lines gave deviations. The used acceleration voltage of 25 kV is 3 times higher than the *K*- energies of cobalt and iron, thus the fluorescence of the *K*-lines should be fully excited. Also they are better separated in the *K*-range. Normally, the standard evaluation algorithm in the SEM is optimized for bulk samples with dimensions in the micrometer range in depth whereas we investigated very thin wires/bars with diameters of some tenth of nanometers. The higher energetic *K*-lines are weighted assumed that the scattering volume of a bulk sample is given and thus are overestimated, whereas the *L*-lines are less energetic thus the lower back scattering power rightly weighted.

1.4 X-ray absorption near-edge structure and extended X-ray absorption fine structure spectroscopy

X-ray absorption near-edge structure (XANES, Figure S5) and extended X-ray absorption fine spectroscopy (EXAFS, Figure S6) measurements were performed at the beamlines 01C1 and 17C1 of the National Synchrotron Radiation Research Center (NSRRC, Hsinchu, Taiwan). The spectra of the Co_2FeGa nanowires were collected using the transmission mode. The EXAFS spectra $\chi(k)$ were extracted using the AUTOBK program [13]. The ATOMS program [14] was used to prepare the structural input for FEFF6 [15].The final data analysis was performed using the IFEFFIT program package [16, 17]. The EXAFS fits were carried out at the Co and Ga edges in the *k* range of 2.5–12 Å^{-1} with a k^3-weighting in order to achieve a similar resolution for

comparison. The calculated theoretical models include Co_2FeGa compounds of different structures ($L2_1$, $A2$, $B2$). In the EXAFS fits, only single scattering paths are considered. The fits are carried out in the distance-range of $1.0 - 3.0$ Å. In the EXAFS equation [18]:

$$\chi(k) = \frac{1}{k} S_0^2 \sum_{i=1}^{\infty} \left(\frac{N_i}{R_i^2} \cdot \exp(-2\sigma^2 k^2) \cdot \exp\left(\frac{-2R_i}{\lambda(k)}\right) \cdot |f_i(k)| \cdot \sin(2kR_i + \Phi_i(k)) \right)$$

the term $2kR$ in the sine function results from the phase shift of the photoelectron as it leaves the absorbing atom, backscatters from an atom at position R, and returns. The additional phase shift $\Phi_i(k)$ arises because the photoelectron travels through the spatially varying potentials of the absorbing and backscattering atoms. For this reason, the *Fourier* transformed (FT) peaks, as shown in Figure S6, are always shifted by about 0.5 Å from the positions that corresponds to the true interatomic distances. In the case of EXAFS from simple structures such as monoatomic systems, the phase-shift correction can be calculated theoretically using the complex scattering function by the program FEFF (IFEFFIT). For complicated structures such as ternary *Heusler* compounds, the accuracy of the phase correction by the program cannot be confidently justified. Therefore, the FT spectra are presented without phase shift correction, see e.g. [19-21].

1.5 TEM techniques

Transmission electron microscopy, electron holography

For transmission electron microscopy (TEM) investigations, isolated Co_2FeGa nanoparticles and nanowires were obtained by dissolving silica using NaOH (4M) solutions. The suspended nanoparticles were washed by centrifugation (4000 rpm for 20 min) until the supernatants become neutral and were collected by a final centrifugation of 8000 rpm for 20 min. The obtained nanoparticles were re-dispersed in methanol. Several drops of the solutions were loaded on carbon coated copper grid and transferred to the microscope after complete dryness. The Quantifoil S7/2 (100-mesh hexagonal) copper grids were covered with 2 nm carbon film (Quantifoil Micro Tools, Jena, Germany). The lacey grid used in Figures S8a and d was delivered by PLANO GmbH, Wetzlar, Germany. For electron holography measurements isolated

single Co$_2$FeGa nanowires were chosen in order to avoid magnetic interactions with neighboring nanoparticles or nanowires. Elemental mapping (Figure S7) and two-dimensional (2D) electron holography (Figure S8) were performed by a CM 200 FEG/ Lorentz at 200 kV (FEI, Eindhoven, Netherlands) equipped with a biprism operating at 140 V, a Multiscan 600HP 1k slow-scan CCD camera and a Gatan Imaging Filter 678 (Gatan, Pleasanton, CA, USA). High resolution TEM (HRTEM) and electron holography were performed with a FEI Tecnai F20/Cs-corrected TEM at 200 kV acceleration voltage equipped with a 2k Slow-Scan CCD-camera (Gatan, USA). The analyses of the TEM images were realised by means of the Digital Micrograph software (Gatan, USA). Examples of TEM images of SBA-15 silica are presented in Figures S2b and S2c. HRTEM image of the Co$_2$FeGa nanowire is given in Figure 1b.

Elemental mapping with Energy Filtered TEM (EFTEM)

As the atomic structure analysis of the HRTEM images suggests (Figure 1), a ca. five to ten nanometer thick layer consisting of iron oxide (magnetite) is present at the surface of the Co$_2$FeGa *Heusler* nanowire. In addition, we can assume that this layer is also responsible for the magnetically dead layer observed by EHT (e.g. Figure 2). In order to prove this finding, the composition of the *Heusler* nanowires was investigated by electron energy loss spectroscopy (EELS) and EFTEM using the three-window method. The EEL spectra (Figure S7a) reveal core-loss peaks at iron ($L_{2,3}$ edges), cobalt ($L_{2,3}$ edges), and oxygen (K edge). The elemental maps (Figures 1g and S7b) visualize the distributions of these three elements inside a representative NW, which were obtained by the three-window method in EFTEM imaging mode using the parameters as listed in table Figure S7d. They show in particular an iron concentration till to the surface and an oxide concentration pronounced at the surface (Figure S7c) confirming the existence of the iron oxide layer.

Two-dimensional (2D) electron holography

Figure S8 shows the electron holographic results of three typical nanowires. Their holograms are depicted in Figure S8a, b and c, respectively. The nanowire A shown in image S8a is shorter

(300nm) then nanowires B and C (> 1µm length) shown in S8b,c. Additionally, nanowire A is hanging in between two carbon strings of a lacey carbon TEM grid, whereas nanowires B and C are lying on thin carbon films. The corresponding holographically reconstructed phase images are depicted in S8 d, e and f. Their magnetic stray fields outside the wires are visualised by the overlaid equi-phase lines. As expected the short NW A reveals a much weaker magnetic field (please note the differently scaled color bar for image d). In order to evaluate the internal magnetic induction, phase profiles (S8 g, h and i) were taken normal to the nanowires long axes. According to the *Ehrenberg–Siday–Aharonov–Bohm* effect, the enclosed magnetic flux inside the wires causes a phase difference of the electron wave on both sides outside of the nanowire (see Eq. 2 in the main text). Therefore, from the phase gradient in the profiles, we can get an estimation for the enclosed magnetic induction inside the three nanowires of B_A= 0.3T, B_B= 1.1T and B_C= 0.8T, respectively. Assuming a round cross section of the wires instead a rectangular one, we obtain B_A'= 0.3T, B_B'= 1.3T and B_C'= 1T. Presumably, the field inside the pure *Heusler* compound might be even higher, if the findings of magnetically dead surface layers described in the main text are taken into account. Thus, we obtain *B*-fields in the range of 1T to 1.3T for the long nanowires, which, considering the error of that measurement, agree well with the value gained from the tomographic reconstruction (1.15T).

Holographic tomography

Electron holographic tomography (EHT) was performed with a FEI Tecnai F20/Cs-corrected TEM at 200 kV acceleration voltage equipped with a 2k Slow-Scan CCD-camera (Gatan, USA). For *Lorentz* mode the objective lens was switched off and the aberration (Cs) corrector was used in pseudo *Lorentz* Lens mode at a biprism voltage of 450 V and a field of view of about 560 nm and an excitation of 82 % of the diffractive lens. A Fischione MODEL 2040 dual-axis tomography holder with a maximal tilt angle of about ±70°, combined with 360° in-situ specimen rotation was used to acquire the tilt series. EHT consists of three steps: first, the

acquisition of an electron hologram tilt series (movie 1); second, the holographic reconstruction of the electron object wave from the holograms, to yield a tilt series in both amplitude and phase images (movie 2); and third, the tomographic reconstruction of the three-dimensional (3D) isosurface potential and inner electrostatic potential from the phase tilt series (movie 3). For the acquisition of the electron hologram tilt series, tilting steps of 2° was chosen ranging from about +63° to -67°. For every hologram an empty hologram was recorded in order to eliminate lens distortions and *Fresnel* fringes. The empty hologram was recorded on a free and empty place of the 2 nm thick carbon film and in a certain distance (several microns) away from the magnetic object in order to avoid influence of magnetic stray fields. The same procedure was applied to the flipped sample. Thus, in total about 260 holograms were recorded and processed.

A typical hologram showed about 30 % fringe contrast around the object and about 16 % within the object. Acquisition time amounted 2 seconds with about 400 counts per pixel with a relative standard deviation of about 25%. The fringe periodicity amounted to about 1.5 nm which gives a lateral resolution of about 5 nm in the reconstructed phase image. The experimental realization of EHT requires additional alignment steps (e.g. by cross-correlation or fiducial marker alignment) of the phase tilt series to remove lateral displacements and to identify the (projected) tilt axis before the tomographic reconstruction. A particular problem in EHT arises, if the phase shift due to the object potential is larger than and hence exceeds the maximum interval in a phase image which was initially computed from the reconstructed object wave. Therefore, specific 2D phase unwrapping algorithms (e.g. branch-cut algorithm) have to be applied, to retrieve the full specimen-induced phase shift. For the tomographic reconstruction procedure, several advanced algorithms have been developed. The latter include different sampling, regularization and matrix inversion schemes as applied for the 3D reconstruction of the magnetic stray field (Figure 5 of main text).

1.6 Fidelity of EHT reconstructions

Missing wedges in tomograms are inherent to most electron tomography techniques, which causes not only a lower resolution but also artefacts. Therefore, e.g. we recently developed
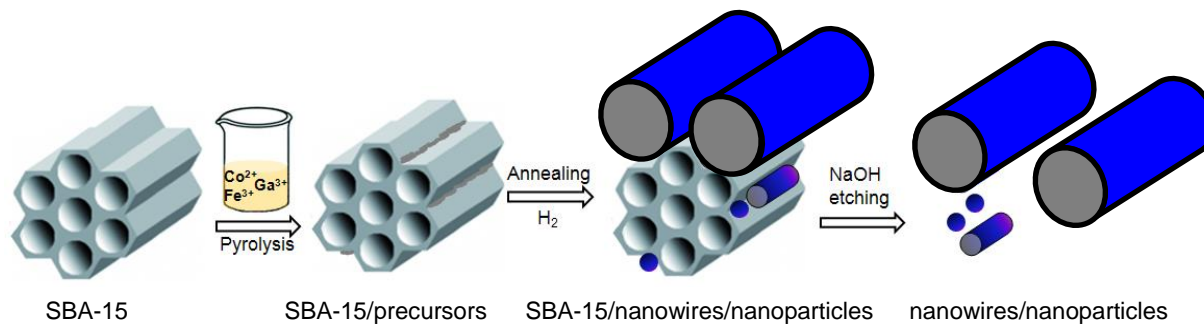
methods for solving the missing wedge problem by exploiting symmetries of suitable objects (n-fold symmetry of cross-section in azimuthal direction) [22,23]. However, since the *Heusler* NW cross-sections do not provide such symmetries, these methods could not be applied here. Hence, we analyzed and partially corrected for the missing wedge influence in the procedure as illustrated in Figure S9: The essence of this approach is to generate a test object to analyze the missing wedge artefacts of the experimental tilt range combined with the tomographic reconstruction technique used (in our case W-SIRT). The test object is generated by applying a threshold on the experimental tomogram (Figure S9a) and setting the internal distribution (higher than threshold) to unity (Figure S9b). The result is forward projected and again reconstructed with the same parameters as for the experimental data to obtain the tomogram of the test object (Figure S9c). The experimental tomogram (Figure S9a) can then be divided by the tomogram of the test object to partially correct for missing wedge artefacts leading to the "corrected" tomogram (Figure S9d). Especially, variations inside the NW caused by the missing wedge are reduced, and the absolute value is increased as supported by the line profiles (Figures S9e,f). Another indication of the reliability of such a partial correction is the signal modulation visible in the *Fourier* transform of the corrected tomogram in the missing wedge region that nicely fits with the object modulation in the azimuthal range covered by the experimental tilt range.

Artefacts caused by diffraction contrast appear in the 2D projections at certain tilt angles of the tilt series, where the nanowire is oriented close to zone axis. For tilts with very pronounced artefacts, these can be locally replaced with more reliable data from adjacent tilt images. By comparing experimental projections with corresponding ones computed from the reconstructed tomogram we can estimate, whether the error amplification of the artefacts remaining is acceptable. The SI Figure S10 shows such a comparison on a representative projection at 1 degree tilt: It reveals that the area with diffraction contrast (green arrow) is not visible in the projection computed from the tomogram, as the difference image supports. Therefore, it is reliable to conclude that regions suffering from diffraction contrast do not result in significant artefacts in the tomogram considering the specific parameters of our reconstruction, such as number of iterations and weighting filter.
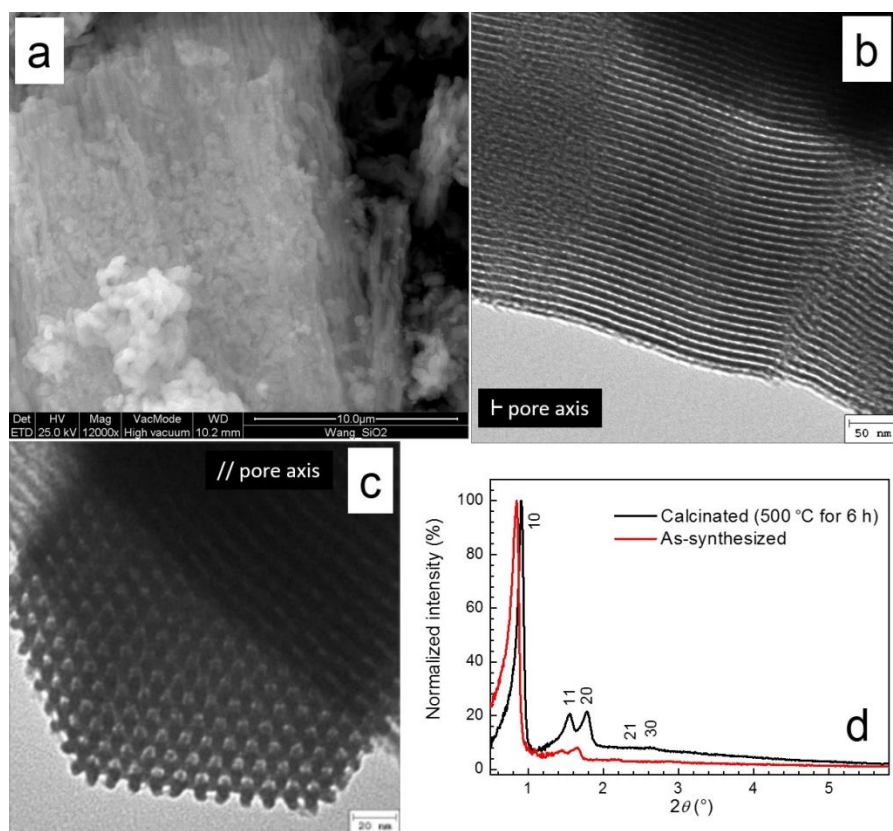
22.12.2015

References for supporting information

[1] W.S. Jung, *Bull. Kor. Chem. Soc*. 25, 51 (2004).

[2] M. Gellesch, M. Dimitrakopoulou, M. Scholz, C.G.F. Blum, M. Schulze, J. van den Brink, S. Hampel, S. Wurmehl, B. Büchner, *Cryst. Growth Des.* 13, 2707 (2013).

[3] D.Y. Zhao, Q.S. Huo, J.L. Feng, B.F. Chmelka, G.D. Stucky, *J. Am. Chem. Soc.* 120, 6024 (1998).

[4] A.J.C. Wilson (ed.), International Tables for Crystallography, Vol. C, Kluwer Academic Publisher, Dordrecht/Boston/London, 1992, p. 428.

[5] M.F. Toney, S. Brennan, *Phys. Rev. B* 39, 7963 (1989).

[6] C. Maunders, J. Etheridge, N. Wright, H.J. Whitfield, *Acta Cryst. B* 61, 154 (2005). Program *CELSIZE*, Version 1.1 (1995). Freeware available via Homepage of *International Union of Crystallography.*

[7] K.H.J. Buschow, P.G. van Engen, R. Jingebreur, *J. Magn. Magn. Mater.* 28, 1 (1983); Inorganic Crystal Structure Database (ICSD), FIZ Karlsruhe, Germany, code 102386.

[8] K.H.J. Buschow, P.G. van Engen, *J. Magn. Magn. Mater.* 25, 90-96 (1981); Inorganic Crystal Structure Database (ICSD), FIZ Karlsruhe, Germany, code 102385.

[9] L.G. Akselrud, Y. Grin, *J. Appl. Crystallogr.* 47, 803 (2014).

[10] J.-F. Bérar, P. Lelann, *J. Appl. Crystallogr.* 24, 1 (1991).

[11] A.A. Levin, S.K. Filatov, P. Paufler, R.S. Bubnova, M. Krzhizhanovskaya, D.C. Meyer, *Z. Kristallogr.* 228, 259 (2013).

[12] R.A. Young (Ed.), 'Introduction to the Rietveld method', IUCr Book Series, Oxford University Press, 1993.

[13] M. Newville, P. Livins, Y. Yacoby, J. J. Rehr, E. A. Stern, *Phys. Rev. B* 47, 14126 (1993).

[14] B. Ravel, *J. Synchr. Rad.* 8, 314 (2001).

[15] S.I. Zabinsky, J.J. Rehr, A. Ankudinov, R.C. Albers, M.J. Eller, *Phys. Rev. B* 52, 2995 (1995).

[16] M. Newville, *J. Synchr. Rad..* 8, 322 (2001).

[17] M. Newville, B. Ravel, B.D. Haskel, J.J. Rehr, E.A. Stern, Y. Yacoby, *Physica B* 208, 154 (1995).
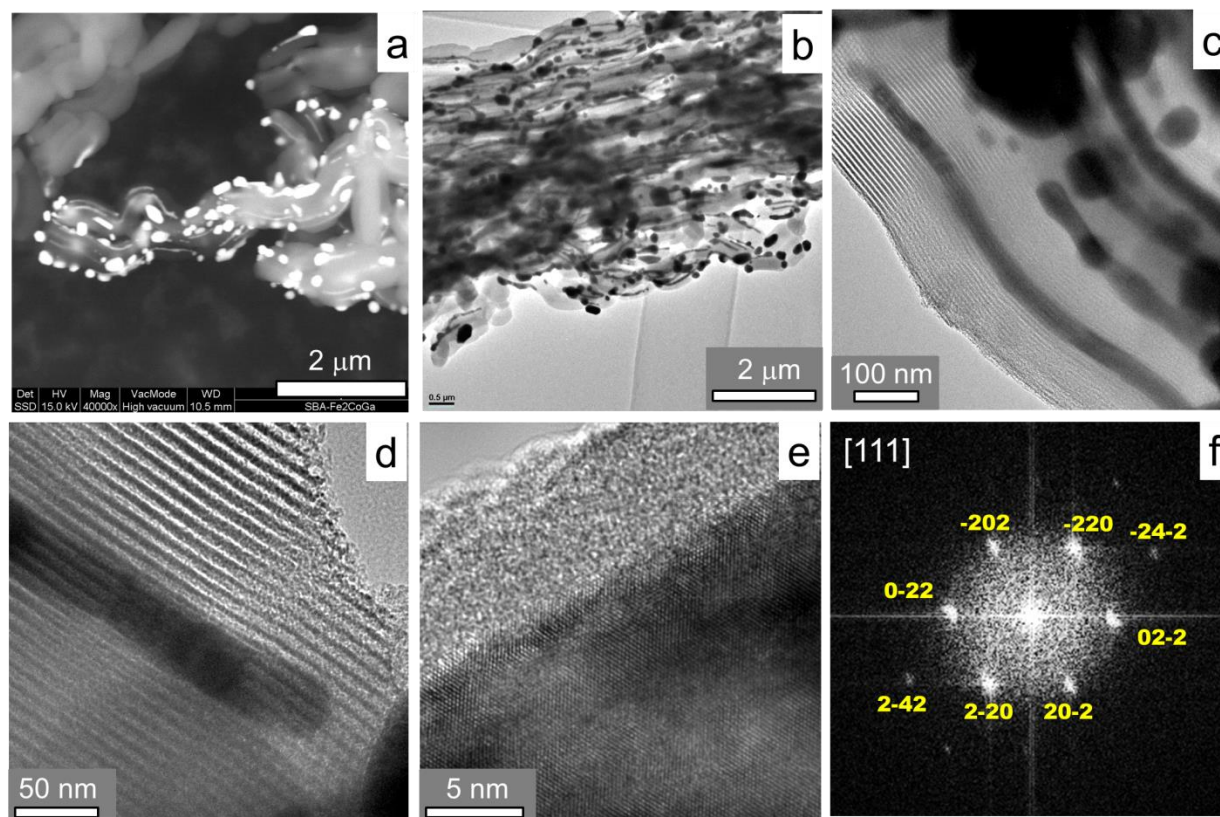
[18] E.A. Stern, *Phys. Rev. B* 10, 3027–3037 (1974).

[19] B. Balke, S. Wurmehl, G.H. Fecher, C. Felser, M.C.M. Alves, F. Bernardi, J. Morais, *Appl. Phys. Lett.* 90, 172501/3 (2007).

[20] C. Wang, F. Casper, Y. Guo, T. Gasi, V. Ksenofontov, B. Balke, G.H. Fecher, C. Felser, Y.-K. Hwu, J. Lee, *J. Appl. Phys.* 112, 124314 (2012).

[21] C. Wang, F. Casper, T. Gasi, V. Ksenofontov, B. Balke, G.H. Fecher, C. Felser, Y.-K. Hwu, J.-J. Lee, *J. Phys. D: Appl. Phys.* 45, 295001 (2012).

[22] A. Lubk, D. Wolf, P. Simon, C. Wang, S. Sturm, C. Felser, *Appl. Phys. Lett.,*105, 173110 (2014).

[23] A. Lubk, D. Wolf, P. Prete, N. Lovergine, T. Niermann, S. Sturm, H. Lichte, *Phys. Rev. B,* 90, 125404 (2014).

Figure S1. *Schematic illustration of the chemical synthesis of the Co_2FeGa nanowires. Channels and external surfaces serve as template for the growth of the one dimensional structures.*

Figure S2. *Morphology SEM (a) and TEM (b and c) images and normalized SAXS patterns (d) of SBA-15 silica. (b) Side view of channels and (c) top view showing hexagonal order. (d) X-ray diffraction indicating hk indices of the hexagonal plane SBA-15 lattice.*
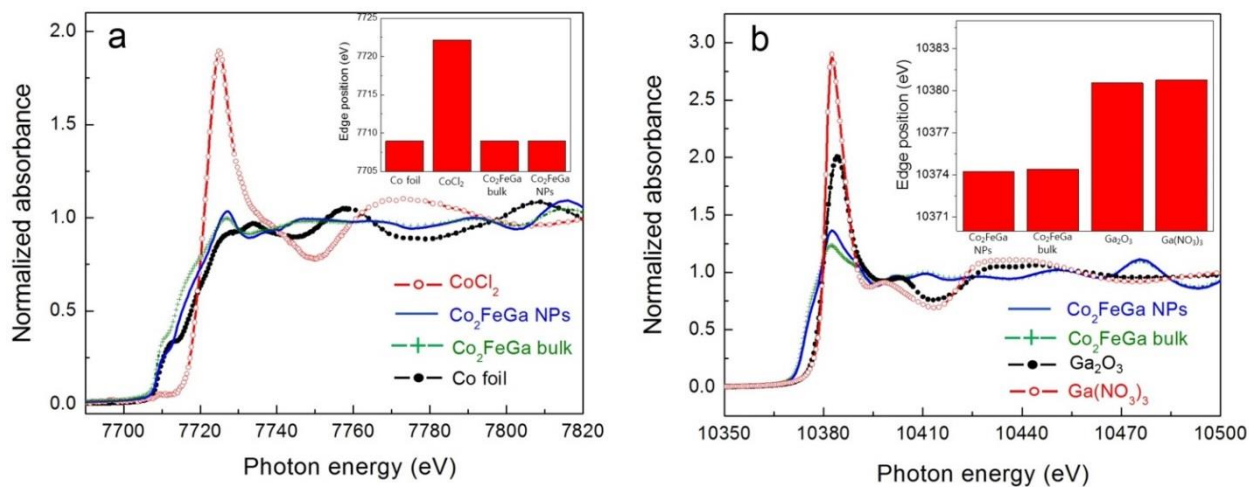
Figure S3. *SEM (a) and TEM (b,c,d,e) images illustrating the growth process of Co$_2$FeGa on the SBA-15 templates. (f) shows the diffractogram (FFT) of the HRTEM image (e) indicating [111] zone.*
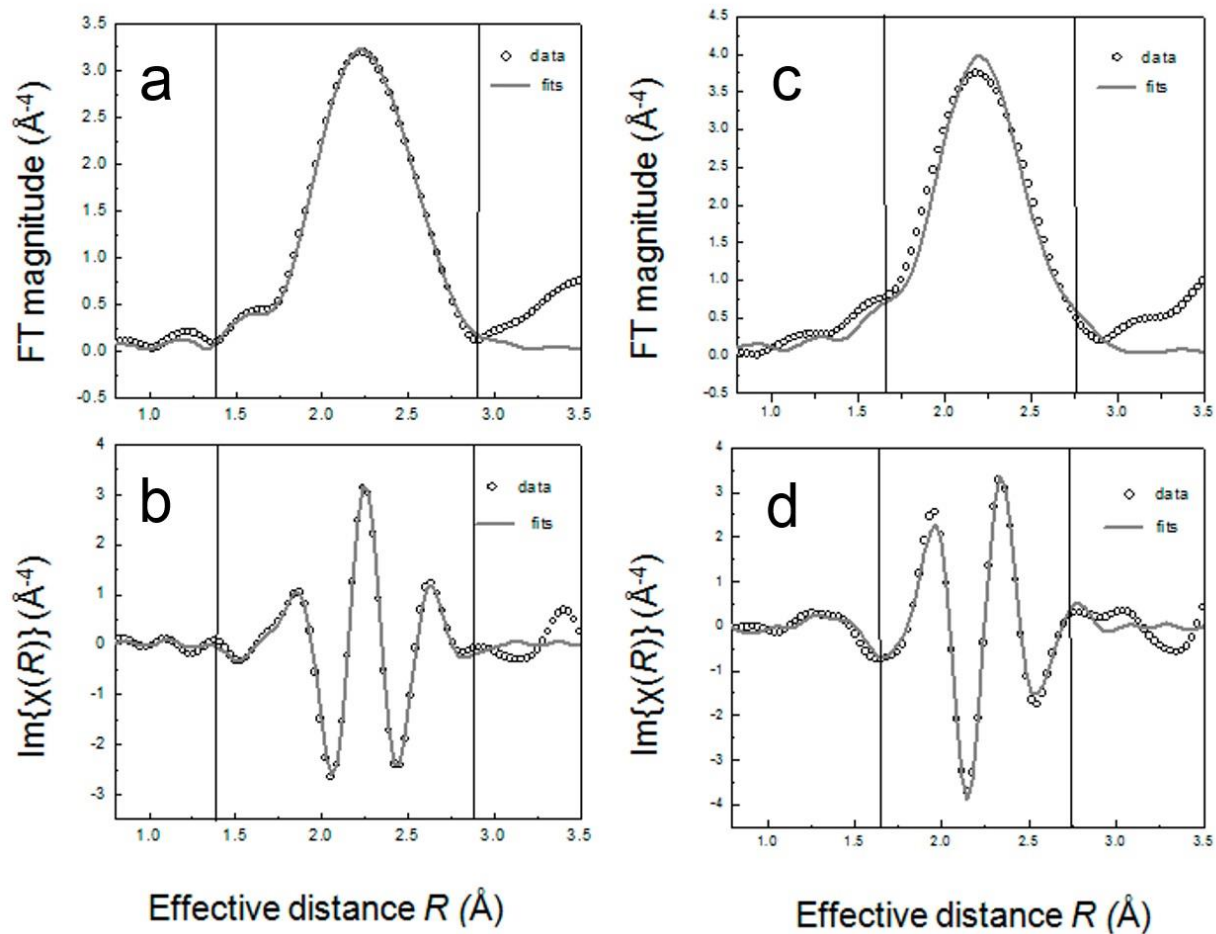
Figure S4. *SEM micrograph and EDX spectrum of Co₂FeGa nanowire. The SEM image obtained by backscattering mode is shown in (a). The corresponding EDX spectrum of the nanowire indicated in (a) by an arrow is shown in (b). About 19 individual nanowires were measured indicating almost an ideal chemical composition of Co₂FeGa.*
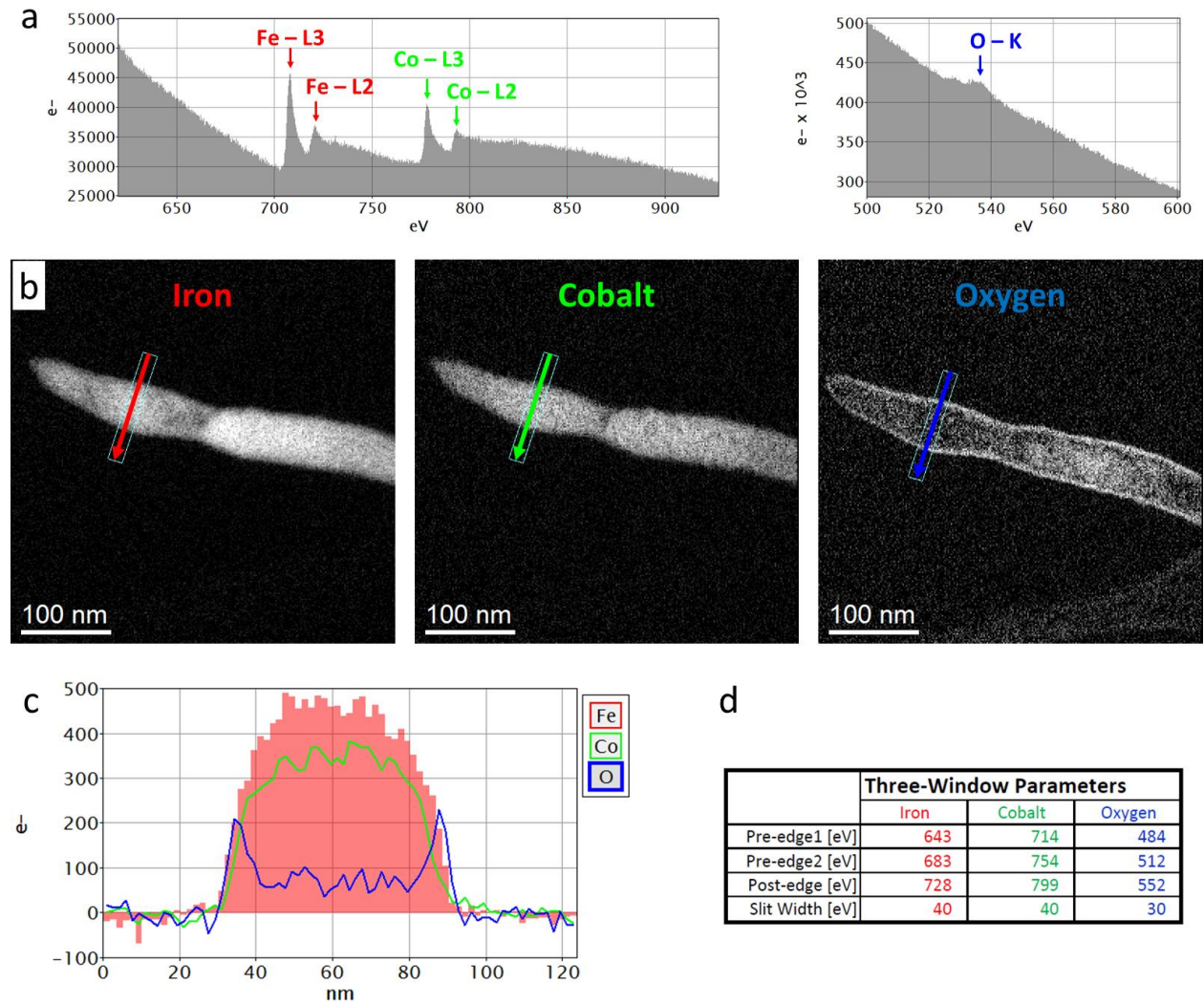

Figure S5. *The XANES spectra of Co₂FeGa nanowires at the K-edges of Co (a) and Ga (b). The data for different reference samples including the foil, precursor, and bulk Co₂FeGa are also shown for comparison. The insets in Figures (a) and (b) show the edge positions of the samples derived from the first deflection point of the spectra. In both edges, Co₂FeGa nanowires exhibit the same edge positions that connect to the oxidation states of the probed elements confirming the absence of oxidation of Ga in Co₂FeGa nanowires.*
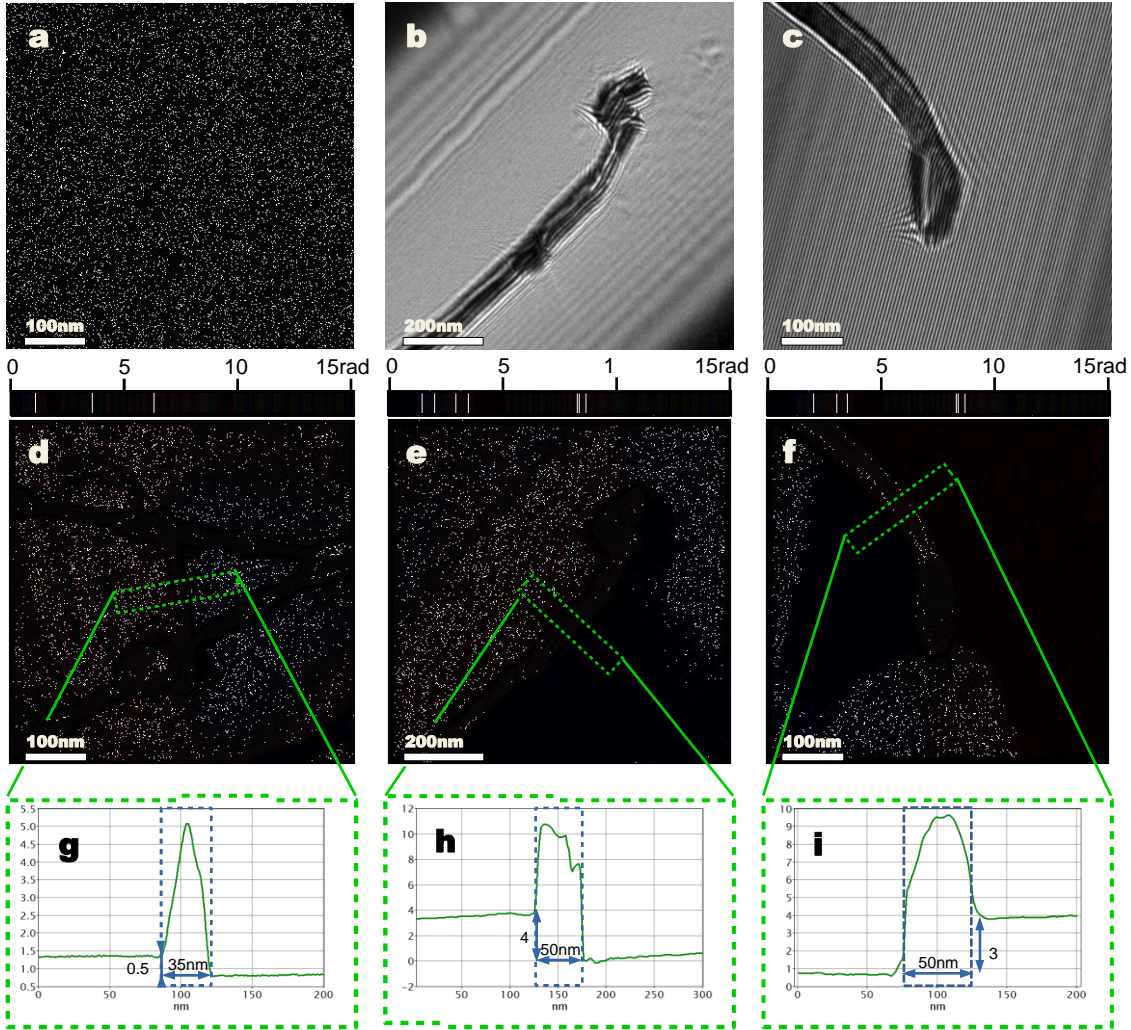
Figure S6. *The EXAFS data and fits of Co₂FeGa nanowires at the K-edges of Co and Ga. The magnitudes and imaginary components of Fourier transforms of EXAFS spectra are shown in (a), (b) for Co and (c), (d) for Ga. The fits (shown as solid lines) are based on L2₁-type ordered Co₂FeGa model. The shown spectra are not corrected for the phase shifts (for details, see text section 1.4).*
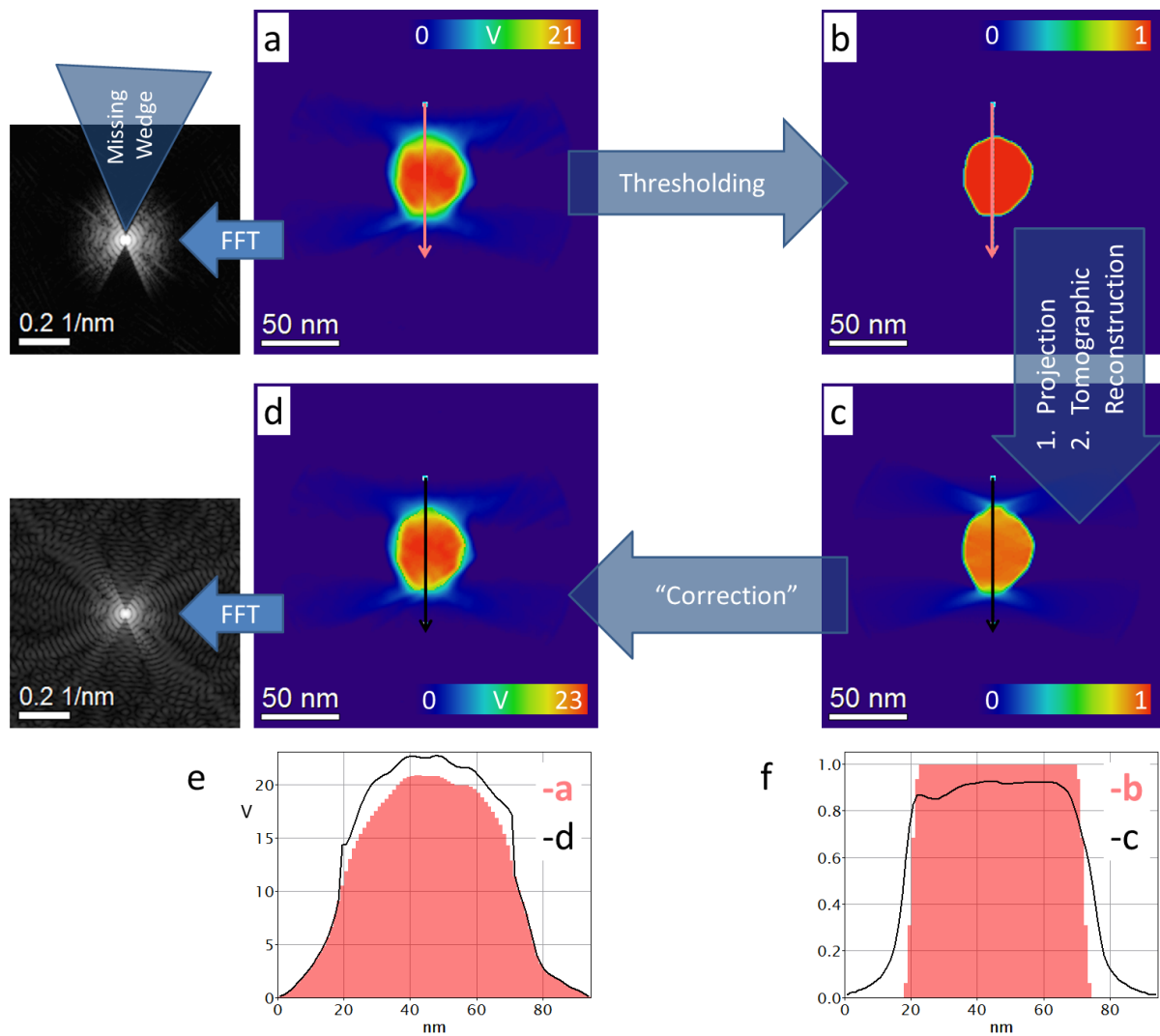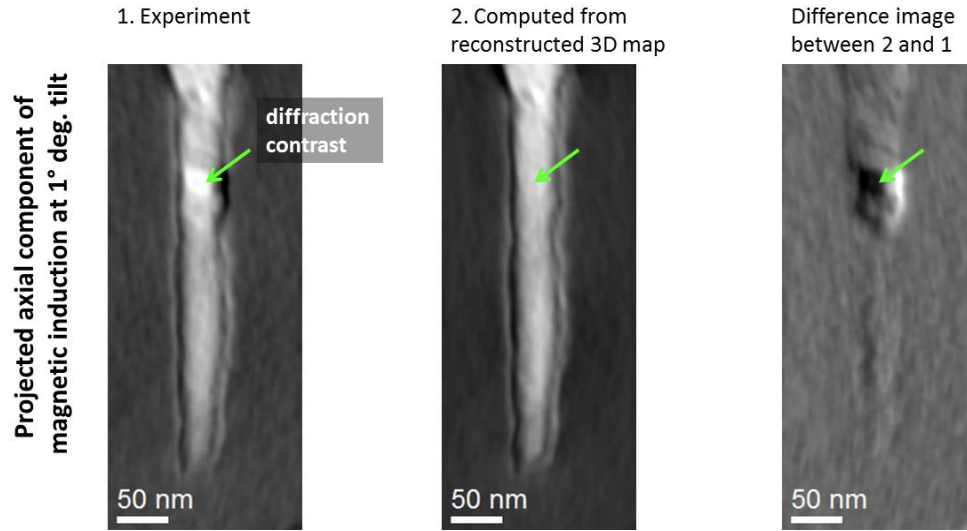
Figure S7: *EELS and EFTEM analysis on Co₂FeGa Heusler nanowires. (a) EEL spectra with core-loss peaks at cobalt, iron and oxygen due to inner-shell ionization events. (b) Elemental maps obtained by the three-window method in EFTEM imaging mode. (c) Line profiles across the NW at positions indicated by the arrows in (b). (d) Acquisition parameters of the three window method used for elemental mapping.*

Figure S8. *2D electron holography revealing the magnetic stray fields of three different Co₂FeGa nanowires: (a,b,c) holograms of nanowires, namely A, B and C, respectively. (d,e,f) Color coded reconstructed phase of (a,b,c), respectively. Color bar displays phase shift in radians (please consider the differently scaled color bar for image (d), due to weaker magnetic stray field). Overlaid equipotential lines (black) of 0.2 rad illustrate the stray fields, following the magnetic field lines. (g,h,i) profiles normal to the nanowires as indicated by the green dotted boxes in d,e,f.*

Figure S9: *Procedure for analysis and partial correction of missing wedge artefacts in the experimental tomogram on the example of a Heusler NW. The experimental tomogram (a) (cross-section of the NW) and its FFT, where the missing wedge is clearly visible, runs through a threshold procedure to generate a test object (b). The test object is projected and reconstructed in the same way as the experimental data to compute the tomogram (c). The experimental tomogram (a) is then divided by (c) to partially correct for missing wedge artefacts leading to the "corrected" tomogram (d). (e,f) Line profiles according to the arrows in (a-d).*

Figure S10. *Comparison of experimental and processed phase images at 1 degree tilt. Left: Projection from experiment. The area affected by the diffraction contrast is marked with a green arrow. Center: Projection computed from the tomogram. The artefact caused by diffraction is removed. Right: Difference image displays pure diffraction contrast.*